A Revised Real-Time Multivariate MJO Index

PING LIU,* QIN ZHANG,+ CHIDONG ZHANG,# YUEJIAN ZHU,@ MARAT KHAIROUTDINOV,* HYE-MI KIM,* COURTNEY SCHUMACHER,& AND MINGHUA ZHANG*

* *School of Marine and Atmospheric Sciences, Stony Brook University, Stony Brook, New York*
+ *Climate Prediction Center, NOAA/NWS/NCEP, College Park, Maryland*
# *Rosenstiel School of Marine and Atmospheric Science, University of Miami, Miami, Florida*
@ *Environmental Modeling Center, NOAA/NWS/NCEP, College Park, Maryland*
& *Texas A&M University, College Station, Texas*

(Manuscript received 6 July 2015, in final form 22 October 2015)

ABSTRACT

This study investigates why OLR plays a small role in the Real-time Multivariate (Madden–Julian oscillation) MJO (RMM) index and how to improve it. The RMM index consists of the first two leading principal components (PCs) of a covariance matrix, which is constructed by combined daily anomalies of OLR and zonal winds at 850 (U850) and 200 hPa (U200) in the tropics after being normalized with their globally averaged standard deviations of 15.3 $W m^{-2}$, 1.8 $m s^{-1}$, and 4.9 $m s^{-1}$, respectively. This covariance matrix is reasoned mathematically close to a correlation matrix. Both matrices substantially suppress the overall contribution of OLR and make the index more dynamical and nearly transparent to the convective initiation of the MJO. A covariance matrix that does not use normalized anomalies leads to the other extreme where OLR plays a dominant role while U850 and U200 are minor. Numerous tests indicate that a simple scaling of the anomalies (i.e., 2 $W m^{-2}$, 1 $m s^{-1}$, and 1 $m s^{-1}$) can better balance the roles of OLR and winds. The revised PCs substantially enhance OLR over the eastern Indian and western Pacific Oceans and change it less notably in other locations, while they reduce U850 and U200 only slightly. Comparisons with the original RMM in spatial structure, power spectra, and standard deviation demonstrate improvements of the revised RMM index.

1. Introduction

The Madden–Julian oscillation (MJO; Madden and Julian 1971, 1972) is a dominant mode of tropical atmospheric variability on intraseasonal time scales (Zhang 2005) and substantially modulates global weather and climate (Zhang 2013). How to represent the MJO accurately in theory and models has been a challenge to both research community and operational prediction centers. Early diagnosis of the MJO employed power-spectral analysis (Madden and Julian 1972) or its variant of bandpass filtering (e.g., Weickmann et al. 1985). Composite studies (e.g., Rui and Wang 1990) manually detected individual MJO events on Hovmöller (time–longitude) diagrams constructed with pentad-mean OLR anomalies. Slingo et al. (1996) used the bandpass-filtered zonal-mean zonal wind at 200 hPa to represent the overall intraseasonal variability in 15 AGCMs. Maloney and Hartmann (1998) applied an EOF analysis to the bandpass-filtered zonal wind at 850 hPa to derive an MJO index for a composite life cycle. Such indices usually disclose an MJO well in either winds or convection. Using only one condition, however, is less effective for real-time applications. Bandpass-filtering techniques are also less effective because they produce large distortions on both ends of a time series.

To monitor the real-time MJO evolution in magnitude, phase, baroclinic structure, and convection–dynamical coupling, Wheeler and Hendon (2004, hereafter WH04) developed an all-season Real-time Multivariate MJO (RMM) index. The RMM index consists of the first two normalized principal components (PCs, known as RMM1 and RMM2) of combined daily anomalous OLR and zonal winds at 850 (U850) and 200 hPa (U200); the preprocessing steps are summarized in section 2. The combined EOF analysis can dramatically increase the signal-to-noise ratio of OLR associated with MJO compared to an EOF analysis on OLR only (WH04). Because RMM1 and RMM2 are orthogonal to each other, the square root of their square

Corresponding author address: Dr. Ping Liu, Endeavor Hall 199, SoMAS, Stony Brook University, Stony Brook, NY 11794-5000.
E-mail: ping.liu@stonybrook.edu

DOI: 10.1175/MWR-D-15-0237.1

summation represents the MJO amplitude, and they form a two-dimensional Cartesian phase diagram to describe the eastward propagation of MJO phases with approximate geographical navigations. Such effectiveness and simplicity have made the RMM a standard measure of the MJO to monitor its real-time evolution (Gottschalck et al. 2010), study its dynamics (Wang et al. 2012), validate its model simulations (Kim et al. 2009; Waliser et al. 2009), and verify its operational forecasts (Lin et al. 2008; Zhang and van den Dool 2012; Kim et al. 2014).

There is a notable weakness in the RMM index. Straub (2013) compared the contribution of each field to the index and found that zonal winds play a dominant role while OLR is minor. Wolding and Maloney (2015) also disclosed the relatively small fractional contribution of OLR in comparison to the winds. Consequently, the RMM acts like a dynamical index to most effectively capture the strength of the first baroclinic structure of zonal winds at zonal wavenumber 1, especially during the mature phases of strong MJO events. However, it has tremendous difficulty representing the convective initiation of the MJO. Straub (2013) gave several examples to demonstrate that the RMM index detected many MJO phases in terms of convection that were inconsistent with an index based on bandpass filtering: some occurred too late, some were false alarms, and some were virtually missing. When the RMM index is used to evaluate model simulations and verify operational predictions, it can potentially give a higher score to a model that produces better global-scale MJO signals in winds even with weak local signals in convection or a lack of interaction between convection and circulation.

The weakness of the RMM index can be attributed to a power leakage of some important components in OLR associated with the MJO. Liu (2014) systematically analyzed the partitions of power spectra among all complex EOF (CEOF) modes. The two modes of the RMM index substantially lack the power of MJO convection at zonal wavenumbers 2–5, which corresponds to a weaker-than-observed structure over the Maritime Continent and western Pacific. Such a power leakage is hypothesized as the main cause of the relatively small role played by OLR in the RMM. Although this leakage can be sufficiently restored by using CEOF modes 3–10, it is difficult to incorporate all the first 10 modes into the simple Cartesian phase diagram. Other more effective approaches are needed.

In this spirit, several indices were designed recently. Kikuchi et al. (2012) separated the intraseasonal oscillation into two modes and designed a bimodal representation of the oscillation. Both modes were projections onto the extended EOF of bandpass-filtered OLR during boreal winter and summer. This separation strengthens MJO signals in winter compared to those in the RMM index, partly because more OLR information was included. Based on OLR alone, Kiladis et al. (2014) combined bandpass-filtered and nonfiltered anomalies to design two univariate indices of the MJO to track its convective component. They demonstrated that the timing and strength of the MJO are quite disparate from those of the RMM index when convective signals are of primary interest. Thus, they advocated the use of OLR-based metrics for retrospective analyses of individual MJO cases and for validating model simulations. By completely dropping the OLR, Ventrice et al. (2013) incorporated the velocity potential at 200 hPa instead to develop a velocity potential MJO (VPM) multivariate index. This index best captures larger-amplitude MJO signals during boreal summer. The velocity potential deemphasizes convective signals of the MJO over the Indian Ocean warm pool and enhances MJO signals over the relatively dry longitudes of the equatorial eastern Pacific and Atlantic.

These efforts to develop alternative MJO indices illustrate a continuing need to assess and improve the RMM index in capturing MJO characteristics. This need motivates the present study to investigate possible improvements of the RMM index to better represent MJO convection. Section 2 introduces the data and relevant method used and reviews the steps to develop the RMM index. Section 3 presents the mathematical basis for deriving the RMM modes from four relevant matrices, and compares their spatial patterns, power spectra, and standard deviations. A revised RMM index based on a partially scaled covariance matrix is then introduced. Section 4 employs the revised RMM index to represent four typical and widely discussed, or even controversial, MJO events from initiation to strengthening and eastward propagation so as to demonstrate its notable improvements over the original RMM. Section 5 summarizes the results and discusses immediate applications with the revised RMM.

2. Data and procedures for the RMM index

WH04 designed several steps to prepare the three fields for CEOF analysis. They first removed the seasonal cycle represented by the first four harmonics of the annual cycle from daily OLR from NOAA satellite observations (Liebmann and Smith 1996) and U850 and U200 from the NCEP–NCAR reanalysis (Kalnay et al. 1996). These data have 2.5° × 2.5° grid spacing and span from 1 January 1979 to the present, while the subset of years 1979–2001 were used for the CEOF analysis. WH04 subtracted the interannual variability, which is a

TABLE 1. Four real symmetric matrices for RMM and their scaling factors.

Name	Meaning	Scaling factors
RMM	Covariance scaled	Globally averaged std dev: 15.3 for OLR, 1.8 for U850, and 4.9 for U200
CORR	Correlation	Std dev of time series on each grid
COV	Pure covariance	Nonscaled or equivalently with all 1
RMM-r	Covariance revised	2 for OLR, 1 for U850 and U200

regression onto the first rotated EOF (REOF) mode of SSTA in the Indo-Pacific domain of 55°S–60°N, 30°E–70°W (Drosdowsky and Chambers 2001). The short record of SSTA, however, cannot make the regression statistically stationary and different results would occur when newer data are added, as indicated by Liu (2014) who used the SSTA derived from the Hadley Centre Sea Ice and Sea Surface Temperature dataset (HadISST; Rayner et al. 2003). WH04 then removed the linear trend and variations at frequencies lower than interannual scales, which are well represented by a 120-day retrospective average. Lin et al. (2008) indicated that this retrospective average can effectively reduce both the interannual and lower-frequency variability. Several operational centers, including the Climate Prediction Center at NOAA, have been using this simplified approach to preprocess the daily anomalies. Our tests show that the sensitivity of the derived RMM index to this approach is overall smaller than that to the SSTA regression. We adopt this simplified method in this study. Finally, WH04 smoothed a large portion of tropical synoptic waves by averaging the resultant anomalies between 15°S and 15°N. We recognize that Kiladis et al. (2014) effectively reduced the lower-frequency background as well as some higher-frequency waves in OLR by subtracting a 40-day running mean and then smoothing with a 9-day mean.

Right before the CEOF analysis, each of the OLR, U850, and U200 anomalies was normalized by dividing their globally averaged STDs of 15.3 $\mathrm{W\,m^{-2}}$, 1.8 $\mathrm{m\,s^{-1}}$, and 4.9 $\mathrm{m\,s^{-1}}$, respectively, for an equal contribution to the eigenvectors and then to the RMM. We will reason mathematically below that this procedure is a scaling rather than a conventional normalization compared to a correlation matrix and a nonscaled covariance matrix. More importantly, we will show that the OLR is overly scaled even in the correlation matrix such that it plays a minor role in the resultant RMM, while it is overly dominant in the nonscaled covariance matrix. This motivated us to seek a differently scaled covariance matrix to develop a revised RMM. Many symmetric matrices were derived and compared while four closely relevant ones are described in Table 1.

TABLE 2. Explained-to-total variance in percentage by the first two CEOF modes and the difference of the second and third CEOF modes.

	CEOF 1	CEOF 2	CEOF 2 − CEOF 3
RMM	13.4	12.3	6.2
CORR	12.3	11.0	5.3
COV	10.9	9.5	3.0
RMM-r	10.6	9.7	3.5

It is noteworthy that the fractional contributions of each field on each geographical grid and globally have been used to assess the contributions to the RMM for a long period. This technique is based on the fact that the fractional contributions are the inner products of two vectors: one consists of the two components from each field or its values over a geographical grid and the other is formed by RMM1 and RMM2. Since the total summation eventually amounts to the amplitude of RMM as $\sqrt{\mathrm{RMM1}^2 + \mathrm{RMM2}^2}$ and nonnegative definite, each contribution was scaled by this amplitude to compute the percentage contribution from a long-term mean. In the original RMM, OLR contributes only 17% or so to the RMM, which was concluded to be very low (Wolding and Maloney 2015). This technique can be misleading because one or two contributions at a given time can be negative in a phase behind the RMM and such conditions abound (Wolding and Maloney 2015). The negative values of each field may not represent the actual contribution, as the percentage of a number is commonly computed over the sum of several numbers with the same sign. Although the absolute values of each inner product appear to be better for the arithmetic, their summations would no longer amount to the RMM amplitude. How to make such fractional contributions consistent with the variance partitions in the CEOF analysis is under investigation. Consequently, we did not use this fractional assessment to determine the scaling factors, instead we adopted the variance share of reconstructed anomalies to the raw as it is positive definite to produce a solid percentage (see Table 2).

In power-spectral and relevant analyses, we will define the MJO as signals at bands of 30–100 days and wavenumbers 1–5 in eastward propagation, the equatorial Rossby (ER) waves at the bands of 6–50 days and wavenumbers 1–10 in westward propagation, and the equatorial Kelvin waves at 2.5–30 days and wavenumbers 1–14 in eastward propagation. These two

waves are the main remnant in the anomalous time series and they play an important role to the MJO dynamics (e.g., Roundy 2015), so we include them in our analysis. The band definitions and filtering mostly follow Wheeler and Kiladis (1999), and slight variations to them do not alter the conclusions.

To compare the occurrences and intensity for strong MJO phases represented by the RMM and RMM-r indices (see Table 4), eight phases are divided evenly and each occupies 45° on the RMM phase diagram. The angle is defined by the arctangent of RMM2 over RMM1 in degrees and a negative value is converted to positive by adding 360°. As an example, phase 1 is located in the half-open range of (180°, 225°]. The RMM1 is generally nonzero so all angles are defined. Each phase corresponds empirically to a geographical range. For example, phases 1 and 2 cover Africa and the central Indian Ocean where MJOs usually initiate (e.g., Madden and Julian 1972). A point determined by the RMM1 and RMM2 values moves from lower to higher phases as a tracer for the eastward evolution of an MJO.

3. Comparison of RMM modes from four matrices

a. Mathematical basis

EOF analysis (e.g., Lorenz 1956) is a classical approach to separate leading modes as dominant signals from meteorological fields that expand in both space and time. The core of the analysis computes eigenvalues and constructs eigenvectors of a real symmetric matrix whose elements are either a covariance or correlation coefficient between the time series of each grid pair in the domain of interest. Elements on the main diagonal correspond to the variance in a covariance matrix or 1 in a correlation matrix. Both matrices are positive semidefinite mathematically and have two salient features to make EOF analysis unique: 1) the eigenvalues are nonnegative and their summation is the same as the trace (summation of the main diagonal elements), and 2) its eigenvectors (usually normalized) are orthogonal and form a complete set of basis to reconstruct the original time series. These eigenvectors are invariant in time and constitute dominant patterns of the field. A covariance matrix has more physical meaning in deriving an RMM index than a correlation matrix because its eigenvalues are a redistribution of the total variance and their descending order quantifies the relative importance from most to least of each mode to the original field.

Mathematically, two real (vs complex) symmetric matrices have different sets of eigenvalues and eigenvectors if they are not identical after being manipulated with elementary operations. A correlation matrix is generally not equivalent to a covariance matrix, since each correlation element comes from the time series normalized with a different STD and elementary matrix operations cannot convert one to the other. Because the anomalous daily series of OLR, U850, and U200 are different, their combination can construct a covariance matrix quite different from a correlation matrix and thus with distinct sets of eigenvalues and eigenvectors. The order of combination is unimportant since a column or row swap, one of the elementary matrix operations, can manipulate the differently ordered matrix back. A correlation matrix is advantageous to mathematically guarantee an equal contribution from each time series since their variances are all one.

The way to divide the time series with an averaged STD across the domain is equivalent to scaling the series on each grid with the same STD (global-mean STD in the RMM case). The resultant time series are thus different from those subject to conventional normalization except for the one with exactly the same STD as the mean value. Main diagonal elements of the covariance matrix are also equivalently scaled section by section with the square of the three numbers and are less likely to become identical. Consequently, the equal contribution assumption to construct the covariance matrix for RMM appears to be dependent on identical values of summation for each field section. This equality, however, is not fully satisfied by using the globally averaged STDs, which is shown below.

Suppose the global summations of variance have values of a, b, and c for OLR, U850, and U200, respectively. We then need to find three numbers x, y, and z to satisfy

$$a/x = b/y = c/z = (a + b + c)/3. \tag{1}$$

A unique solution can be easily found as $x = 3a/(a + b + c)$, $y = 3b/(a + b + c)$, and $z = 3c/(a + b + c)$. Their square root should be used to scale the time series of each field so as to satisfy Eq. (1). These values can be readily computed from the anomalous time series as $\sqrt{x} = 1.64$, $\sqrt{y} = 0.19$, and $\sqrt{z} = 0.52$. Although they appear to be quite different from the global average STD for each field, the three numbers are roughly 10 times smaller, indicating that the contribution from each field to the total variance is approximately equal. This feature is similar to a correlation matrix that mathematically guarantees an equal contribution from not only sectional but also individual time series. Consequently, a covariance matrix derived using this approach (scaled by either global STD or $\sqrt{x}$, $\sqrt{y}$, $\sqrt{z}$) is different from a conventional covariance matrix but close to a correlation matrix. Since the matrix scaled by $\sqrt{x}$, $\sqrt{y}$, and $\sqrt{z}$ also

produces an index very similar to the WH04 RMM, it is not discussed further in this study. We next compare the eigenvalues, eigenvectors, and MJO in the reconstructed anomalies from the leading modes of the four matrices in order to introduce a revised RMM. These matrices are listed in Table 1 with their short names and scaling factors for each field.

b. Comparisons

We first compare the fractional variance in percentage by each of the first three leading CEOF modes derived from the three matrices that were constructed with nonscaled covariance (COV), correlation (CORR), and scaled covariance by the global STDs (RMM) (Table 1). The values (Table 2) can quantify the relative importance of each mode and whether it can be separable from the rest based on the difference from its neighboring eigenvalues as a criterion proposed by North et al. (1982). The revised RMM (RMM-r) is also listed in the last row of Table 2, while how to obtain its scaling factors of 2, 1, 1 will be discussed later.

Each of the first two CEOF modes explains slightly more than 12% of the total variance in the RMM matrix and slightly less in CORR. While these two matrices have quite different traces (total variances of the three fields), the close fractional variances indicate their potential similarity in eigenvectors and RMMs. The third mode is 6.2% away from the second in RMM and 5.3% in CORR, which is also similar. This amount of difference makes the first two CEOF modes separable from the rest in both matrices based on North et al. (1982).

The nonscaled covariance matrix COV produces the first two leading CEOF modes to explain 10.9% and 9.5% of the total variance, respectively. The values are smaller than those in RMM and CORR, indicating the relatively smaller importance of these two modes. The third mode explains 3.0% less than the second, suggesting the first three modes are less separable from each other compared to RMM and CORR. RMM-r, which scales only the OLR time series with a value of 2 W m^{-2}, improves the second mode in the explained percentage to become more separable from the rest of the CEOF modes (about 3.5% away from the third mode).

These different fractional variances correspond to different spatial patterns of eigenvectors. Each eigenvector consists of three segments for OLR, U850, and U200, respectively. We display the first two eigenvectors for each field in Fig. 1 as in previous studies. The amplitude of each field at a given location indicates its relative contribution since all eigenvectors are normalized. It is noteworthy that the first mode in COV and RMM-r resembles the second mode in RMM and CORR and the second mode in COV and RMM-r resembles the first mode in RMM and CORR (i.e., their orders are switched in Fig. 1). Because the difference between the first and second modes in explained variance is so small, this change does not cause much confusion in physical interpretation. They are scaled together to examine notable differences in spatial patterns.

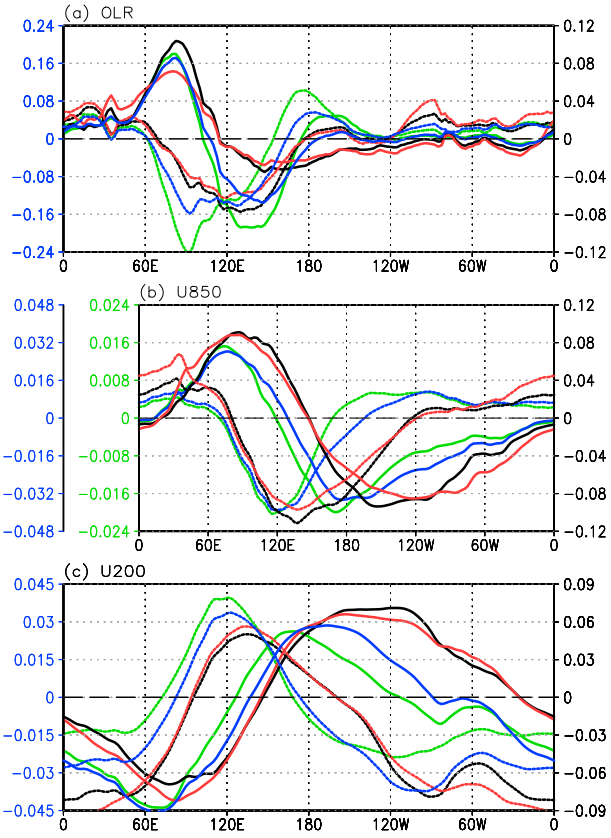

FIG. 1. Spatial patterns (normalized eigenvectors) of the first (solid) and second (dashed) leading EOF modes in the four matrices of RMM (black), CORR (red), COV (green), and RMM-r (blue; the order of first and second is switched; see text for details) for (a) OLR, (b) U850, and (c) U200, respectively.

As anticipated, RMM and CORR generally share very similar patterns in all the three fields, forming one group; COV and RMM-r are also very similar, forming another. For example, in OLR (Fig. 1a), the CEOF1 mode (solid) in all matrices shares close distributions from 150°W eastward to 70°E, representing a nearly identical structure of OLR in that area. So is the case with the CEOF2 (dashed). However, between the Indian Ocean and the date line, RMM-r and COV have much larger OLR magnitude in both CEOF modes than RMM and CORR, suggesting larger OLR amplitude in the reconstructed anomalies and more power spectrum at relevant wavenumbers and frequencies. In U850 and U200, the zero crossings are notably shifted westward in

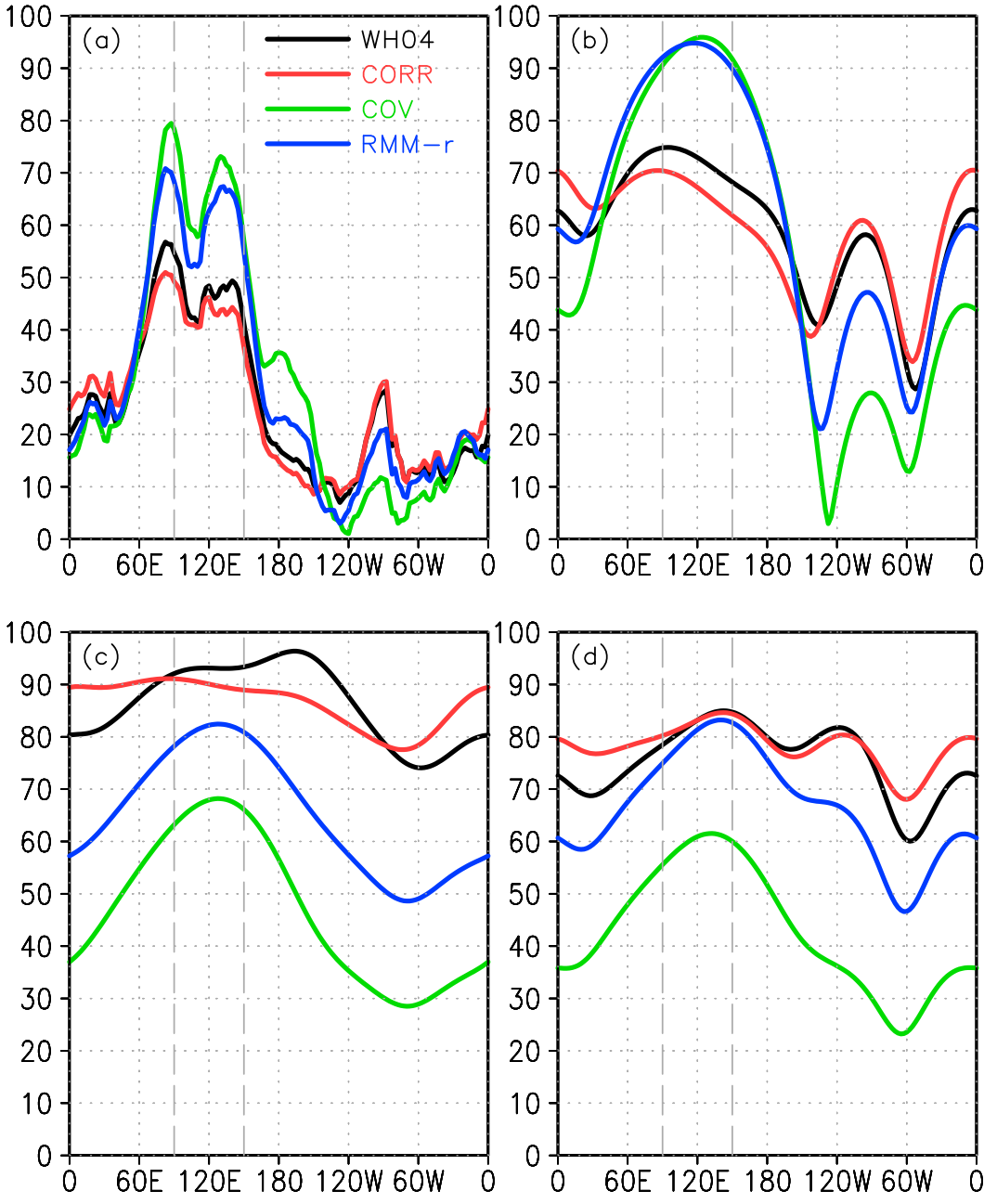

FIG. 2. Percentage contributions of the first two CEOF modes to the total STD in terms of (a) raw OLR, (b) OLR MJO, (c) U850 MJO, and (d) U200 MJO.

RMM-r and COV compared to RMM and CORR. The peak of U200 near 100°W in RMM and CORR shifts westward to 180° as well. Also notable is that U850 has the smallest range in COV and about 30% of that in RMM and CORR, suggesting the smallest contribution to the MJO. Figure 1 indicates that the patterns of all three fields in RMM-r and COV are more concentrated in the Eastern Hemisphere than those in RMM and CORR, which will correspond to enhanced OLR in STD and power spectrum of the anomalies reconstructed from their first two leading modes.

How well the first two leading CEOF modes represent the MJO can be partially assessed by how much their reconstructed anomalies contribute to the STDs of raw OLR and total MJO in the three fields, as shown in Fig. 2. The contribution to the STD of raw OLR (Fig. 2a) indicates that similar patterns are shared by all matrices in most of the region spanning 150°W–60°E, while large

TABLE 3. Intensity and location of strong MJO convective peaks.

	Lon in 2.5°–100°E		Lon in 100°E–180°	
	OLR_m ($W m^{-2}$)	Lon	OLR_m ($W m^{-2}$)	Lon
Raw	−21.0	89.4°	−24.2	131.4°
RMM	−12.6%/60%	90.0°	−12.2%/50.4%	127.4°
RMM-r	−17.0%/81.0%	91.6°	−18.2%/75.2%	128.0°
RMM-raw	8.4	0.6°	12.0	−4.0°
RMM-r–RMM-raw	4.0	2.2°	6.0	−3.4°

differences occur in the rest of tropics. Between 60° and 150°E, CORR contributes least (less than 50%), COV contributes the most with a peak of 80%, RMM-r is very close to COV, and RMM contributes 10%–30% more than CORR but 20%–30% less than COV and RMM-r. The RMM-r creates more balanced contributions than the RMM in OLR.

Figures 2b–d compare the contributions to the STDs of the total MJO by the first two CEOF modes of each matrix. For OLR from 40°E to 150°W (Fig. 2b), CORR contributes least to the total in the four matrices, while RMM contributes about 10%–15% more, but this contribution decreases going eastward, similar to CORR. This rapid dropping of the contribution corresponds to substantial power leakage at zonal wavenumbers 2–5 (Liu 2014). Both COV and RMM-r contribute to the total MJO OLR notably more than the other two, particularly as much as 80%–95% over 60°E–180°. The RMM-r has a maximum contribution near 120°E that is between the two maxima in the RAW (Fig. 2a). This slight difference corresponds to slight deviations in the locations of the convective centers of the MJO (Table 3).

Contributions to total MJO U850 and U200 change places among CORR, RMM, and COV. The two modes of COV contribute least to the total MJO, about 30%–40% less than RMM in U850 (Fig. 2c) and 25% less than RMM in U200 (Fig. 2d). Combined with its greatest contribution in OLR (cf. Fig. 2b), the RMM of COV will be largely a convection-centric index. On the other hand, CORR is overall similar to RMM in both U850 and U200 with a difference within 10%, suggesting that the RMM from CORR is even more dynamical than the original RMM as it contributes least to the MJO in OLR (cf. Fig. 2b). The extreme contributions of the CORR and COV modes provide motivation to seek a more balanced contribution to the STD of total MJO by the three fields. After a series of tests, we find that a combination of $2 W m^{-2}$, $1 m s^{-1}$, and $1 m s^{-1}$ to scale the three anomalous fields before constructing the covariance matrix provides a well-balanced contribution to the total MJO among the three fields, especially in the Eastern Hemisphere. The resultant index is denoted as RMM-r. As indicated in all panels of Fig. 2, OLR in RMM-r is very close to that in COV in key MJO regions, but closer to RMM in other regions in terms of the contributions to the STDs of raw OLR and total MJO. It is very close to RMM in U200 as well and substantially enhanced in U850 compared to COV. The contributions to the total MJO between 90° and 150°E are reduced to be very similar in both U850 and U200 (about 80%–85%). Such balanced contributions from the three fields to the total MJO make the RMM-r a more desirable matrix to derive the RMM index.

This balance is also supported by the wavenumber–frequency power spectrum analysis of reconstructed anomalies from the RMM, COV, and RMM-r modes, as shown in Figs. 3 and 4. Power spectra for each field reconstructed from the RMM modes (e.g., Fig. 11 in WH04) are subtracted to show the improvement. The difference between RMM and COV indicates that COV substantially increases the representation of OLR power at zonal wavenumbers 2–5 by 50%–90%, but suppresses OLR power at wavenumber 1 by 30% (Fig. 3a). It also suppresses the U850 power at zonal wavenumber 1 by 60% (Fig. 3b) and U200 by 70% (Fig. 3c). Consequently, the RMM index of COV is closer to a convection index compared to RMM and CORR. The difference between RMM-r and RMM, however, indicates that RMM-r enhances the OLR power by 40%–80% at zonal wavenumbers 2–5 and produces little changes at zonal wavenumber 1 (Fig. 4a). The RMM-r reduces power by about 20% in U850 (Fig. 4b), but only 10% in U200 (Fig. 4c), suggesting a better-balanced MJO power spectra in the three fields. This is consistent with the contributions to the total STD of MJO (cf. Fig. 2) and also suggests that RMM-r is an improved matrix for the RMM index. Meanwhile, COV enhances equatorial Rossby waves (green curve in the left parts of Fig. 3) by 20% at zonal wavenumbers 2–3 and a 30-day period in OLR (Fig. 3a), while it suppresses equatorial Kelvin waves (green curve in the right part of Fig. 3) by 40% in U850 and U200 at zonal wavenumber 1 and 25 days (Figs. 3b and 3c). RMM-r, in contrast, produces very small changes in these synoptic-scale components (no discernable green curve in Fig. 4).

Corresponding to the larger OLR power spectra, the RMM-r changes the MJO convection centers in both intensity and location, especially over the western Pacific. Table 3 summarizes the long-term mean (May 1979–July 2013) of selected minima of bandpass-filtered OLR in the Indian Ocean (2.5°–100°E) and Maritime Continent–western Pacific (100°E–180°). The separation in longitude makes the comparisons more specific,

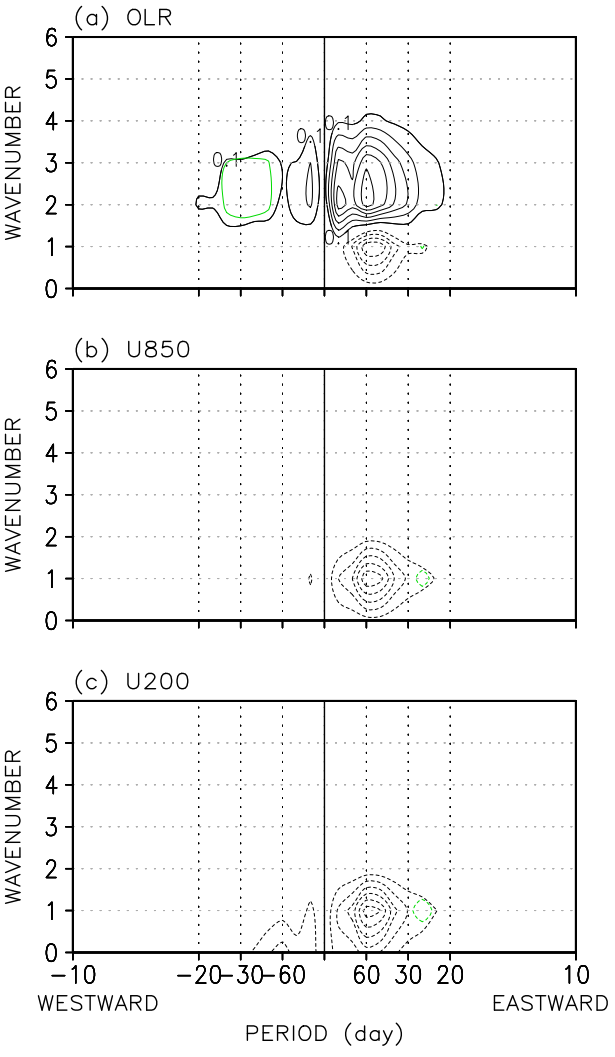

FIG. 3. Differences between COV and RMM in wavenumber–frequency power spectrum of anomalies reconstructed by the first two CEOF modes for (a) OLR, (b) U850, and (c) U200. The intervals are the same as those in the RMM: 0.1 $W^2 m^{-4}$, 0.01 $m^2 s^{-2}$, and 0.1 $m^2 s^{-2}$ for OLR, U850, and U200, respectively. One isoline in each is approximately equivalent to 7%, 11%, and 10%. Green curves are for the equatorial Rossby and Kelvin waves.

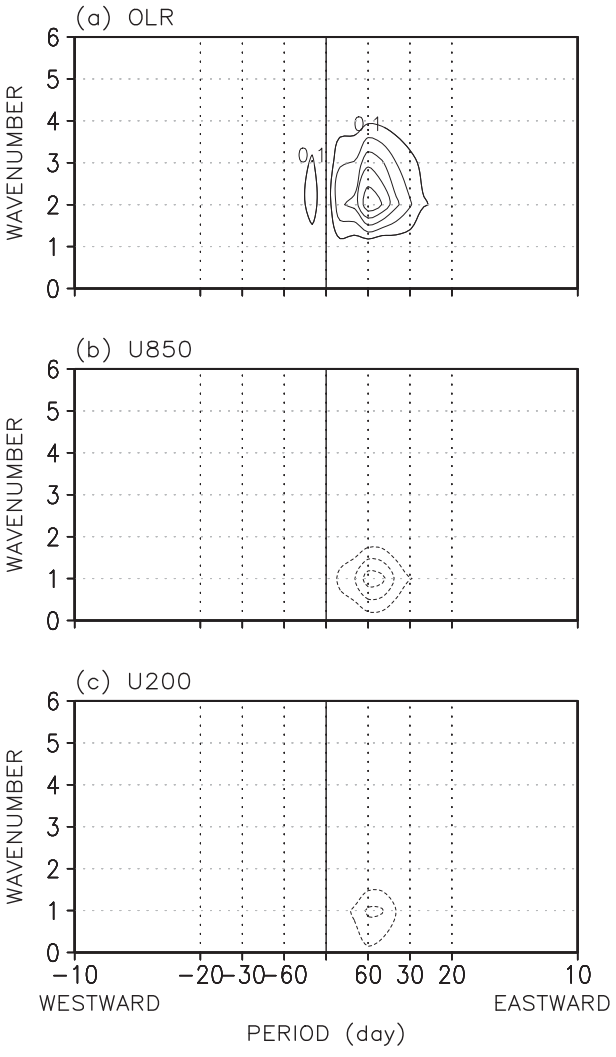

FIG. 4. As in Fig. 3 but for RMM-r.

because MJO convection typically peaks with a minimum OLR over these two sectors separately while some events have only one peak. An estimated total of 525 peaks in each sector correspond to an average of 5 days per event and 3 events in a year during the 35 yr. Tests indicate that 503 peaks would occur in the first sector when using $-17.5\,W\,m^{-2}$ in raw as the threshold and 512 peaks in the second sector with a threshold of $-20.0\,W\,m^{-2}$. These differences are reasonable since a value below the OLR threshold corresponds generally to an MJO peak stronger than moderate (cf. Figs. 5, 7, and 9 below) and a slightly different threshold produces more or less occurrences with similar intensity and locations. The first OLR peak of $-21\,W\,m^{-2}$ is located at 89.4°E and the second peak of $-24.2\,W\,m^{-2}$ is located at 131.4°E. Although these two centers are much weaker than those on the day-to-day maps without any bandpass filtering (cf. the Hovmöller diagrams in section 4), they serve as an objective criterion for the comparison of the RMM and RMM-r. The RMM modes reproduce the first peak at 60% in intensity and about 0.6° to the east and the second peak at 50% in intensity at 4° to the west (third row in Table 3). The RMM-r modes (two rows in bold) increase the first peak to 81% in intensity and the second to 75%. The locations of the RMM-r peaks are about 0.6° closer to the RAW than the RMM modes in the western Pacific but deviate about 1.6° to the east in the Indian Ocean. Such differences in intensity and location agree well with the MJO STD

TABLE 4. Total number (No.) of occurrences and average intensity (AI) for strong MJO phases with RMM magnitude exceeding two normalized units.

	No. of RMM	No. of RMM-r	No. of DIFF%	AI RMM	AI RMM-r	AI DIFF	AI *t* test
Phase 1	217	219	0.9	2.36	2.51	0.15	3.79% | 99.9%
Phase 2	183	227	24.0	2.38	2.40	0.02	0.51
Phase 3	232	269	16.0	2.45	2.44	−0.01	0.59
Phase 4	171	186	8.8	2.48	2.51	0.03	0.18
Phase 5	204	242	18.6	2.50	2.53	0.03	0.32
Phase 6	204	212	3.9	2.38	2.43	0.05	1.18
Phase 7	235	231	−1.7	2.44	2.41	−0.03	1.22
Phase 8	230	292	27.0	2.47	2.54	0.07	1.74% | 90%

distribution (cf. Fig. 2b). The enhanced peaks and the closer location of the peaks in the western Pacific will be further demonstrated in case studies of four MJO events.

The larger fractional STD and power spectra in OLR of the new RMM modes enhance the RMM magnitude $\sqrt{\text{RMM1}^2 + \text{RMM2}^2}$ and increase the number of occurrences for strong MJO phases with amplitude exceeding two normalized units. Table 4 compares the total number of occurrences and averaged intensity for all strong MJO phases during 1979–2013 as detected by the RMM-r and RMM with differences against the RMM. The RMM-r detects more MJO phases and/or stronger magnitudes than the RMM does in nearly all phases, as indicated by the positive values in columns 4 and 7. In particular, it detects 24% more occurrences in phase 2, 16% more in phase 3, 9% more in phase 4, 19% more in phase 5, and 27% more in phase 8. On the other hand, the average intensity from the RMM-r is overall larger than that from the RMM with positive differences in the column 7. Based on the Student's *t* test (column 8), the difference is above the 99.9% significance level in phase 1, above the 90% significance level in phase 8, and insignificant in other phases. The notable changes of phases 1 and 2 in either greater RMM magnitude or larger number of occurrences for strong MJO phases indicate that the RMM-r represents better initiation for the MJOs starting in Africa–western Indian Ocean. This is because the first two phases on the RMM phase diagram correspond to Africa and the western-central Indian Ocean where the MJO is initiated in a composite life cycle (e.g., Maloney and Hartmann 1998). Larger number of occurrences in phases 3–5 will improve the representation of strong MJO phases in the eastern Indian Ocean, across the Maritime Continent, and over the western Pacific. Last, phase 8 has both larger numbers of occurrences and greater average amplitude, which would improve the representation of MJO in the Atlantic basin. These dramatic changes in the number of occurrences and average intensity can be attributed to the overall changes of the EOF structures of RMM-r in the three fields (cf. Fig. 1); they are fundamentally attributed to the new scaling factors of 2, 1, and 1 on the anomalies before the CEOF analysis. The results are mixed with overall smaller differences when all MJO magnitudes exceeding one standard unit are sampled. We next show four cases in which the magnitudes for strong MJO cases in RMM-r agree with the raw better than in RMM.

4. Improvement of RMM-r in several MJO events

Straub (2013) demonstrated several cases of MJO initiation in convection that were nearly transparent to the RMM index and indicated that such cases abounded in past observations. These findings were supported by other recent studies (e.g., Kiladis et al. 2014). In addition to the dramatic changes from Table 4 especially in phases 1 and 2 for the MJO initiation, we choose three typical but distinct MJO events and one controversial event to demonstrate the improvements achieved by the RMM-r in comparison with the original RMM. The analyses include Hovmöller diagrams of the reconstructed OLR anomalies by the RMM modes, MJO amplitude represented by $\sqrt{\text{RMM1}^2 + \text{RMM2}^2}$, and phase evolution on the Cartesian diagram of RMM1 and RMM2. These are the core of the RMM framework. The first two events occurred consecutively during the TOGA COARE field campaign (Webster and Lukas 1992) between 28 November 1992 and 13 February 1993. Their initiation and propagation are quite different and have been intensively studied (e.g., Chen et al. 1996). The third event occurred in 13 December 2006–15 January 2007; it was a short event that was simulated successfully by a global nonhydrostatic cloud-system-resolving model (Miura et al. 2007; Liu et al. 2009). The fourth event occurred during December 2011 when the Dynamics of the Madden–Julian Oscillation (DYNAMO) field campaign (Yoneyama et al. 2013) took place and was not

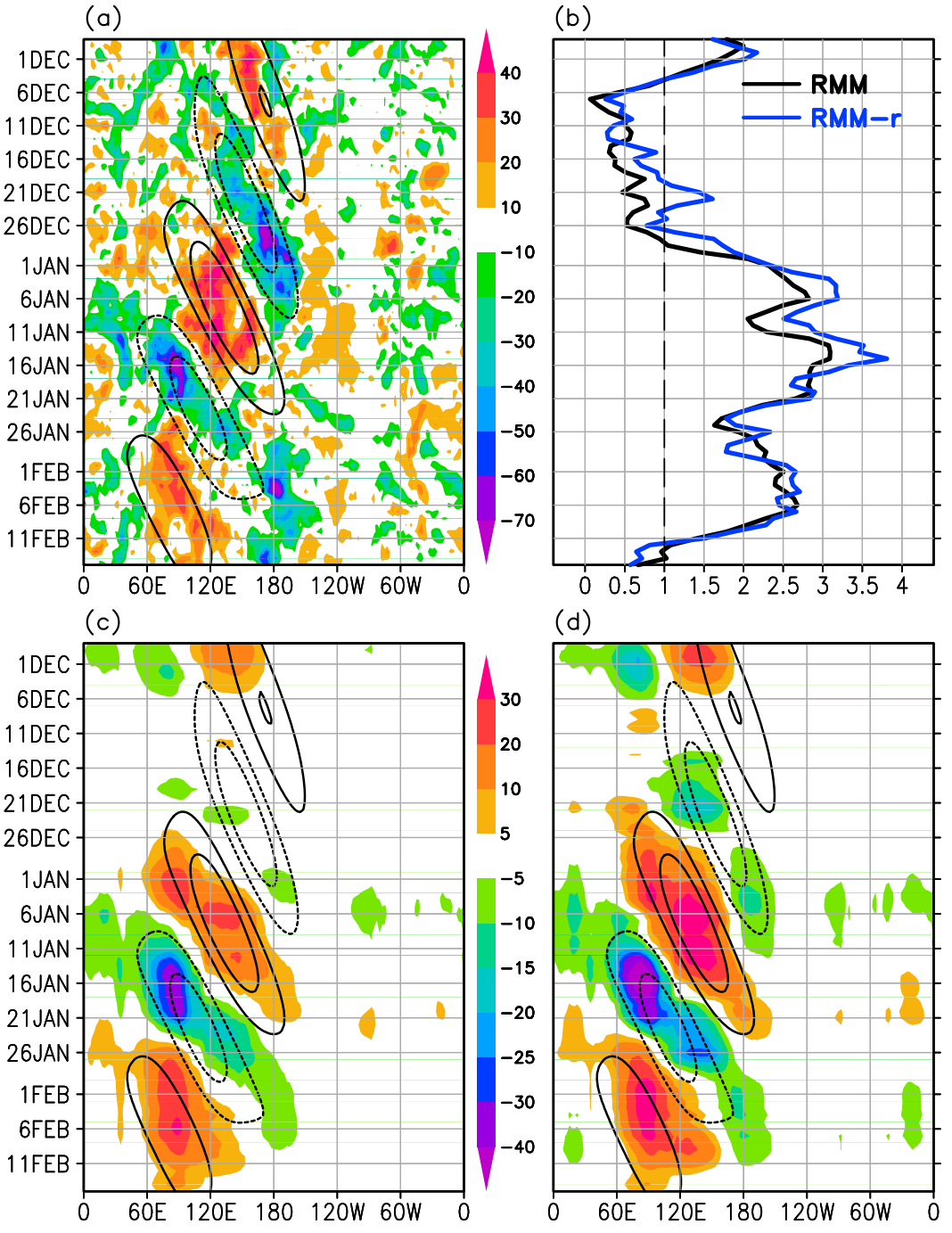

FIG. 5. The two TOGA COARE MJO events between 28 Nov 1992 and 15 Feb 1993 represented by the RMM and RMM-r for (a) raw OLR anomaly (shading) and filtered MJO (contour with interval 10 W m^{-2} and 0 being omitted); (b) amplitudes of RMM (black) and RMM-r (blue); (c) reconstructed anomalies (shading with uneven intervals) by RMM and total filtered MJO [contour as in (a)]; and (d) as in (c), but by RMM-r.

considered an MJO event by the RMM index although other methods did identify it as one. Because U850 and U200 are generally similar in both RMM and RMM-r, we compare primarily the OLR.

The first event during TOGA COARE can be identified on the Hovmöller diagrams of OLR in raw (color shading in Fig. 5a) and total filtered MJO (contours in Figs. 5a,c,d). It started near the end of November 1992 in

the western Indian Ocean. A large dry patch was then embedded in the evolution for about 10 days between 6 and 16 December, causing the wet band to be very narrow. This patch disappeared in the filtered MJO. After this patch, a wet phase redeveloped in the western Pacific and peaked at about 170°E with a magnitude of -50 and $-70\,\mathrm{W\,m^{-2}}$ in raw OLR while the corresponding value was less than half in the filtered MJO (only two contours).

The second event was initiated over Africa and immediately followed the first event. It had two peak phases in raw OLR: one in the central Indian Ocean with a magnitude smaller than $-60\,\mathrm{W\,m^{-2}}$, and the other near the date line of about $-60\,\mathrm{W\,m^{-2}}$. MJO filtering smoothed both centers substantially, probably because the bands up to zonal wavenumber 5 are too narrow to resolve such small-scale peaks. Caution then should be used when forming an index with the bandpass filtering to monitor the peak phases of similar MJO events.

The amplitudes in RMM and RMM-r overall capture both events from their initiation to peak phases (Fig. 5b), while notable changes were made by RMM-r during the first event. Both RMM and RMM-r report an MJO phase between 28 November and 5 December 1992 with amplitudes above 1 normalized unit that then fall below 1 during the next 2 weeks. However, the RMM-r amplitude is greater than 1 again on 18 December, which is about one week earlier than RMM. Between 16 and 25 December, the RMM-r amplitude is nearly twice much as RMM, more consistent with the evolution and magnitude of the peak around 21 December on the Hovmöller diagram (cf. Fig. 5a). For the second MJO event, the amplitudes of both RMM and RMM-r represent its evolution very similarly. A close inspection indicates that RMM-r has two peaks on 5 and 15 January 1993 and they are about 20%–40% larger than the RMM peaks, which is more consistent with the Hovmöller diagram as well.

Changes of RMM amplitudes can also be illustrated by the reconstructed OLR on Hovmöller diagrams (Figs. 5c,d). For the first event, RMM-r (Fig. 5d) has a much larger magnitude in reconstructed OLR than RMM (Fig. 5c), and the duration of the suppressed phase before the redevelopment is much shorter. Consequently, RMM-r is more consistent with the raw for this event (Fig. 5a). For the second event, the reconstructed OLR between 110°E and the date line is about 10–20 $\mathrm{W\,m^{-2}}$ smaller in RMM-r (Fig. 5d) than in RMM (Fig. 5c), suggesting stronger convection in RMM-r and closer to the raw and filtered MJO in Fig. 5a.

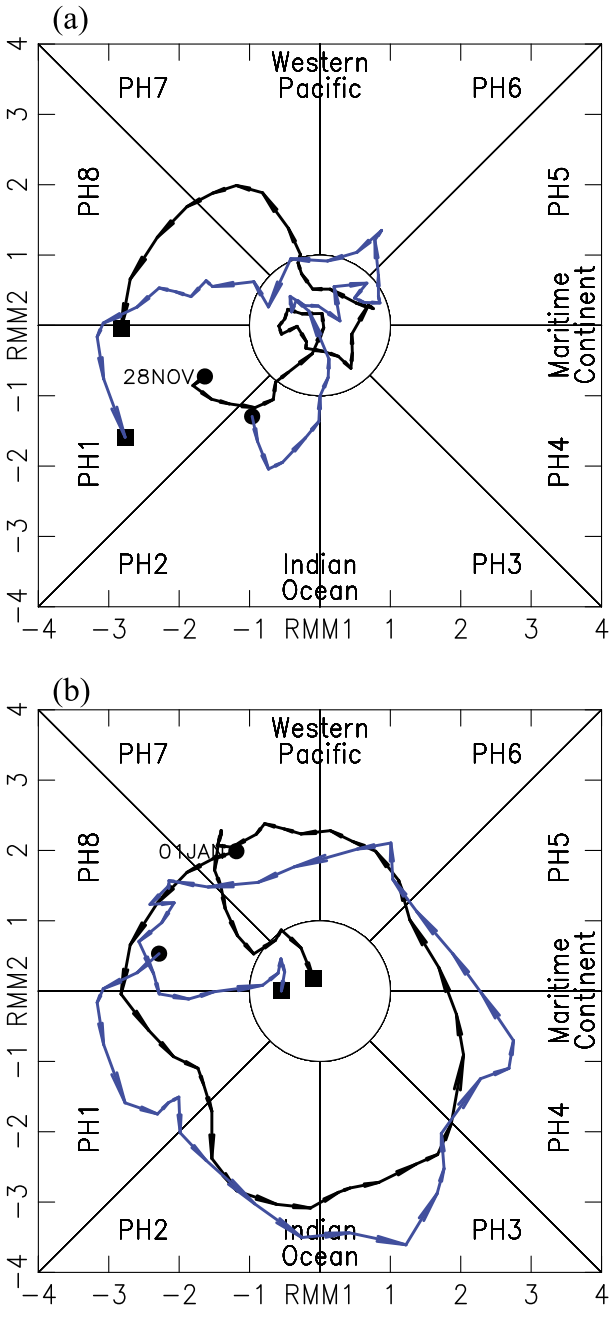

FIG. 6. Cartesian phase diagrams of RMM (black) and RMM-r (blue) for the two events during TOGA COARE (a) 28 Nov 1992–5 Jan 1993 and (b) 1 Jan–15 Feb 1993.

The changes can be demonstrated on the RMM phase diagram, which is the core of the RMM framework for its simplicity and effectiveness. For the first TOGA COARE event (Fig. 6a), RMM-r (blue curve) detects it starting over the western Indian Ocean in phase 2, which is more eastward than RMM (black curve) in phase 1 as shown by the different locations of the two black dots. Such an eastward shift is associated with a 1–2-day lead

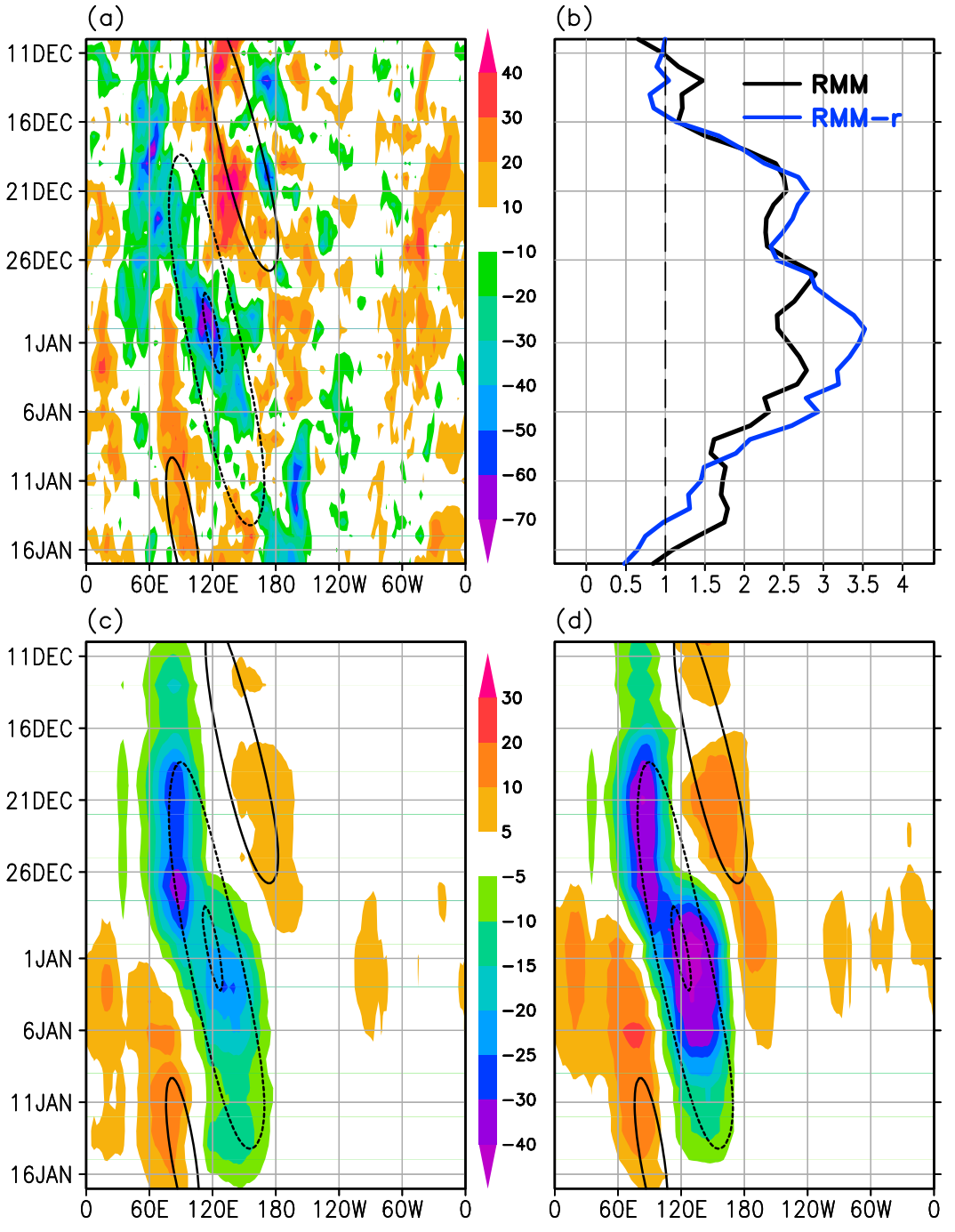

FIG. 7. As in Fig. 5, but for the MJO events during December 2006–January 2007.

of the RMM-r components to the RMM (not shown) and with the westward shift of the RMM-r CEOF structures (cf. blue curves in Fig. 1). The RMM-r remains outside of the unit circle for a few days and enters the circle at the central Indian Ocean, also more eastward and with larger amplitude than the RMM. Later, the RMM-r emerges out of the circle in phase 5 slightly to the east of the Maritime Continent and remains strong for several days toward the end in phase 6 corresponding to the MJO redevelopment (cf. Fig. 5a). This phase evolution of RMM-r is also in a better agreement with the raw OLR than that of RMM. The enhanced OLR variance in RMM-r obviously contributes to the change (cf. Fig. 2). The RMM amplitude is larger than RMM-r in most of phases 7 and 8, which are probably due to a larger contribution of U850 and U200 (cf.

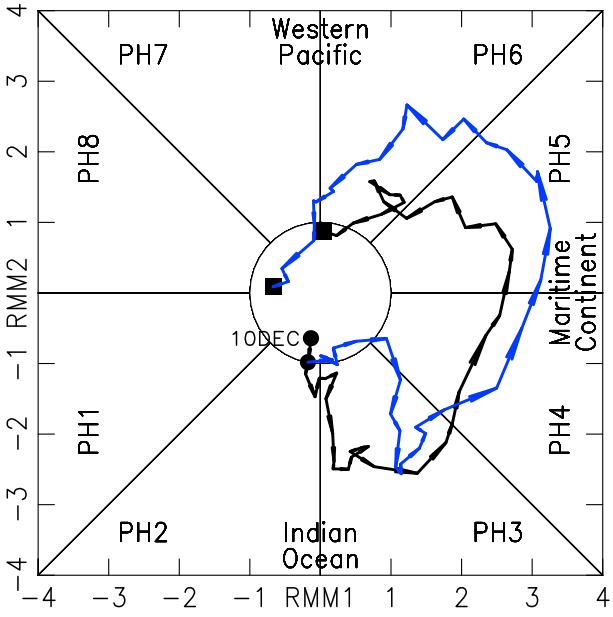

FIG. 8. As in Fig. 6, but for the MJO event during 10 Dec 2006–17 Jan 2007.

Fig. 4). For the second event during TOGA COARE, both RMM and RMM-r represent its evolution well (Fig. 6b). There are still a couple of notable changes in the RMM-r. It peaks in phases 3 over the eastern Indian Ocean and phase 4 over the Maritime Continent, while RMM peaks only once over the central Indian Ocean. The RMM-r amplitude is larger than RMM in phases 1–5. Clearly RMM-r is more consistent with the actual MJO evolution.

Analysis of the third MJO event (Figs. 7 and 8) indicates that RMM-r detects its location more accurately for the convective initiation and has larger amplitude in later phases than RMM. This event started on 10 December 2006 over the western Indian Ocean but strengthened about one week later at 70°E, which is shown on the Hovmöller diagrams of raw OLR (shading in Fig. 7a), filtered MJO (contours in Figs. 7a,c,d), and reconstructed OLR anomalies by the RMM modes (shading in Fig. 7c) and RMM-r modes (shading in Fig. 7d). The phase diagrams of both RMM-r and RMM capture the initiation between phases 2 and 3 (block dots in Fig. 8). Later, the event detected by the RMM-r is much stronger in phases 4–6, more consistent with the Hovmöller diagrams. Such better consistency can also be attributed to the stronger OLR (cf. Fig. 7d) represented by RMM-r than by RMM modes.

The fourth event occurred in December 2011 during the DYNAMO field campaign. Whether this event is an MJO is controversial because the RMM phase diagram does not show a consistent eastward propagation (black in Fig. 10) and the RMM is concentrated in phases 4–7, while convection in raw (Fig. 9a) appears to be centered in the central Indian Ocean. Also the reconstructed OLR was too weak with a center of only $-10\,\mathrm{W\,m^{-2}}$ on the Hovmöller diagram (Fig. 9c). Perhaps more importantly, the bandpass filtering with zonal wavenumbers 1–5 does not allocate even a single contour to the convective center to recognize it as an MJO. Nevertheless, the Hovmöller diagram of raw OLR (Fig. 9a) indicates several convection episodes during 9 December 2011 and 5 January 2012 with a strong episode of OLR $< -60\,\mathrm{W\,m^{-2}}$ prevalent for about a week during 20–27 December. This strong negative OLR supports the recognition of the episode as an MJO event by Gottschalck et al. (2013, see their Fig. 11). The RMM-r framework moderately changes the representation to favor this recognition. The RMM-r amplitude (blue in Fig. 9b) indicates that the event with its amplitude above 1 normalized unit starts on 13 December 2011, about 7 days earlier than the RMM. The RMM-r has its peak amplitudes above 2 normalized units for 4 days, corresponding to the stronger convection center of OLR smaller than $-25\,\mathrm{W\,m^{-2}}$. Such a representation by the RMM-r is closer to the raw OLR than RMM. Interestingly, the revised RMM phase diagram (blue in Fig. 10) represents more random evolution of this event.

5. Summary and discussion

This study revises the WH04 RMM index to improve its accuracy in monitoring the initiation, amplification, and propagation of MJO convection. Mathematical reasoning indicates that the covariance matrix (RMM) for the original WH04 RMM constructed by normalizing the three anomalous fields (OLR, U850, and U200) with their globally averaged STDs is close to a correlation matrix (CORR). Both RMM and CORR substantially suppress the contributions of their RMM modes to MJO power in raw anomalous and total bandpass-filtered OLR such that the RMM index is more dynamical and becomes mostly transparent to the MJO initiation in convection (Straub 2013). A covariance matrix (COV) constructed without any form of normalization, however, goes to the other extreme to produce an index that is heavy on convection. Many tests were conducted to find a partially scaled matrix for an RMM index that includes a larger contribution from OLR without decreasing substantially the contributions from U850 and U200. Results show that a covariance matrix constructed by scaling only the anomalous OLR with a value of $2\,\mathrm{W\,m^{-2}}$ can achieve this goal. This matrix (RMM-r) has two leading modes in which the three fields contribute to the total MJO more equally. Because more power in OLR is included in the revised

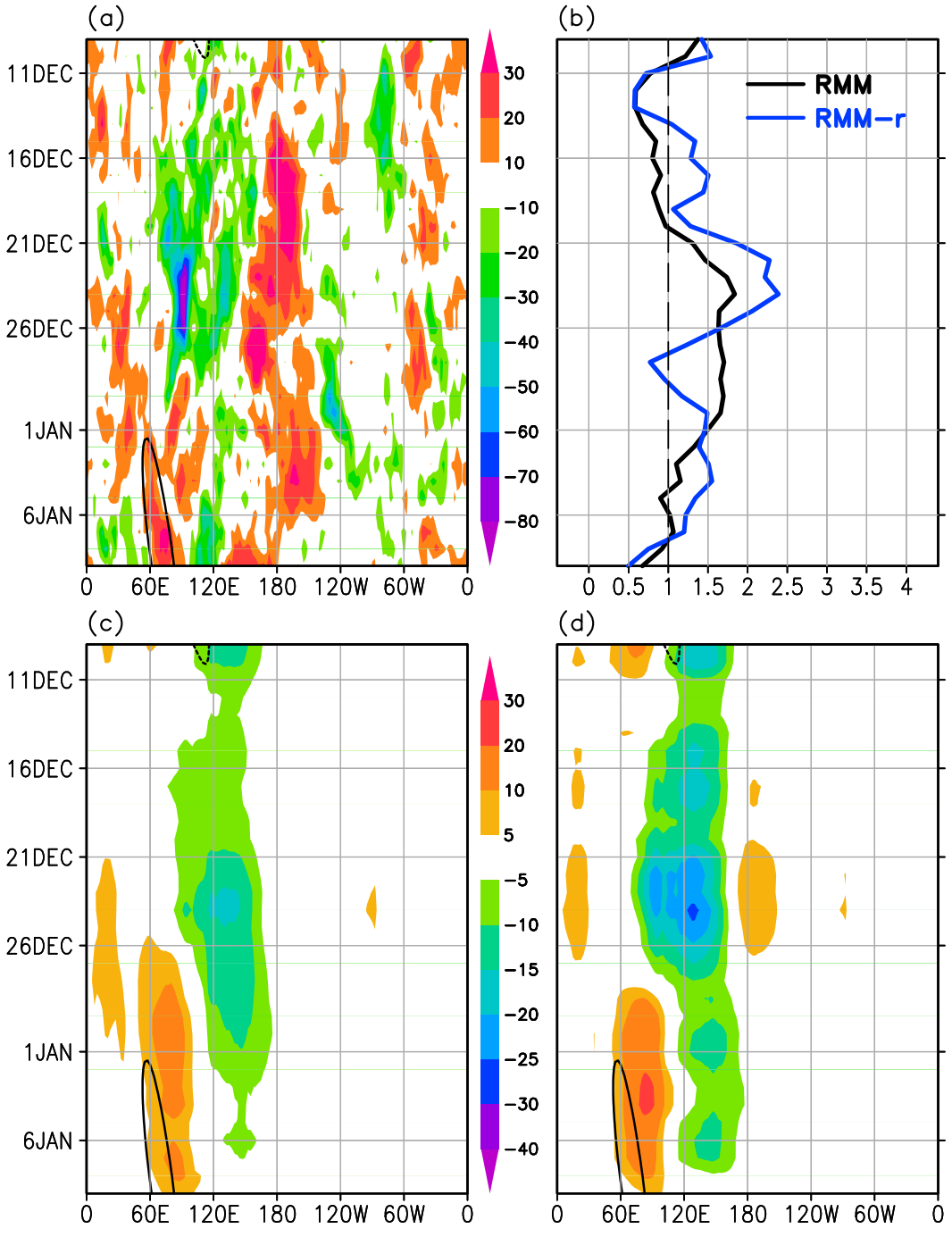

FIG. 9. As in Fig. 5, but for the controversial MJO event during December 2011–January 2012.

RMM, the index can notably better monitor MJO initiation over Africa–western Indian Ocean and later amplification and propagation, especially for its convection over the eastern Indian and western Pacific Oceans. The RMM-r is also more consistent with the raw OLR amplitudes and phase evolutions. The revised RMM is, thus, able to more successfully represent three distinct MJO events and a controversial one during DYNAMO by the simple and effective phase diagram of RMM1 and RMM2. Choosing slightly different values of the scaling (2, 1, and 1) does not change the conclusion. Nevertheless, a combination of optimal scaling factors appears difficult to determine mathematically because it is difficult to determine how much contribution from each field of the RMM modes to the total MJO is ideal, and what the best metric is to estimate the

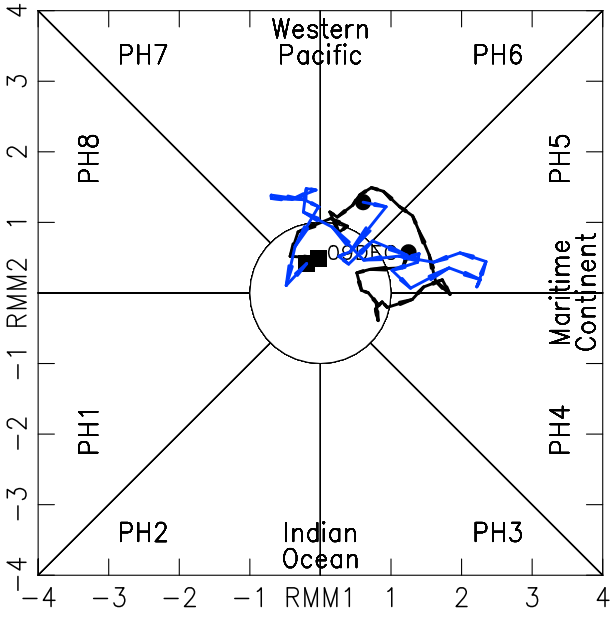

FIG. 10. As in Fig. 6, but for the controversial MJO event during 9 Dec 2011–9 Jan 2012.

contributions accurately. Small deviations from the scaling factors (2, 1, and 1) also produce similar results. While these numbers were obtained empirically by trial and error rather than by either mathematical or physical reasoning, they have added more power of OLR at wavenumbers 2–5 as desired.

Such improvement is also attributable to the mathematical basis of EOF analysis whereby the eigenvalues and eigenvectors are sensitive to the form of its element (e.g., variance vs correlation). A rotated EOF (REOF) approach, however, can hardly make any difference. The REOF cannot transfer much loading from higher-order CEOF modes to the first two, as the original RMM modes already represent about 90% variance of MJO in U850 and U200. Another drawback of REOF is that it will break the orthogonality of the first two leading modes and make them oblique to each other. Either case would make the classical phase diagram of RMM1 and RMM2 less effective and its interpretation difficult.

There are several immediate applications of the RMM-r. Because it is much more responsive to convection than the original RMM, it can be used to examine the issues related to MJO initiation and reveal details of individual MJO events. The RMM from the nonscaled covariance matrix (COV) of the three fields can be used as a good reference to detect MJO convection, especially in its initiation as it represents the MJO most in OLR (90%–95% in power spectrum) and least in U850 and U200 (about 40% in power spectrum). Meanwhile, the more equal contributions from the three fields make the RMM-r more suitable than the original RMM to evaluate MJO simulations by global models and to measure operational prediction skill of the MJO. In addition, the RMM-r is better for the study of convection-centric issues of the MJO, such as its dynamics of convection–circulation coupling and its global impacts.

Acknowledgments. This study is partially supported by the National Weather Service under Grant NA15NWS4680015. Hye-Mi Kim was supported by the Korea Meteorological Administration Research and Development Program under Grant APCC 2013-3141. Minghua Zhang and Courtney Schumacher were supported by the Office of Biological and Environmental Research of the U.S. Department of Energy and by the National Science Foundation. Ping Liu was partially supported by the NSFC under Grant 91437219.

REFERENCES

Chen, S. S., R. A. Houze, and B. E. Mapes, 1996: Multiscale variability of deep convection in relation to large-scale circulation in TOGA COARE. *J. Atmos. Sci.*, **53**, 1380–1409, doi:10.1175/1520-0469(1996)053<1380:MVODCI>2.0.CO;2.

Drosdowsky, W., and L. E. Chambers, 2001: Near-global sea surface temperature anomalies as predictors of Australian seasonal rainfall. *J. Climate*, **14**, 1677–1687, doi:10.1175/1520-0442(2001)014<1677:NACNGS>2.0.CO;2.

Gottschalck, J., and Coauthors, 2010: A framework for assessing operational Madden–Julian Oscillation forecasts: A CLIVAR MJO Working Group Project. *Bull. Amer. Meteor. Soc.*, **91**, 1247–1258, doi:10.1175/2010BAMS2816.1.

——, P. E. Roundy, C. J. Schreck III, A. Vintzileos, and C. Zhang, 2013: Large-scale atmospheric and oceanic conditions during the 2011–12 DYNAMO field campaign. *Mon. Wea. Rev.*, **141**, 4173–4196, doi:10.1175/MWR-D-13-00022.1.

Kalnay, E., and Coauthors, 1996: The NCEP/NCAR 40-Year Reanalysis Project. *Bull. Amer. Meteor. Soc.*, **77**, 437–471, doi:10.1175/1520-0477(1996)077<0437:TNYRP>2.0.CO;2.

Kikuchi, K., B. Wang, and Y. Kajikawa, 2012: Bimodal representation of the tropical intraseasonal oscillation. *Climate Dyn.*, **38**, 1989–2000, doi:10.1007/s00382-011-1159-1.

Kiladis, G. N., J. Dias, K. H. Straub, M. C. Wheeler, S. N. Tulich, K. Kikuchi, K. M. Weickmann, and M. J. Ventrice, 2014: A comparison of OLR and circulation-based indices for tracking the MJO. *Mon. Wea. Rev.*, **142**, 1697–1715, doi:10.1175/MWR-D-13-00301.1.

Kim, D., and Coauthors, 2009: Application of MJO simulation diagnostics to climate models. *J. Climate*, **22**, 6413–6436, doi:10.1175/2009JCLI3063.1.

Kim, H.-M., P. J. Webster, V. E. Toma, and D. Kim, 2014: Predictability and prediction skill of the MJO in two operational forecasting systems. *J. Climate*, **27**, 5364–5378, doi:10.1175/JCLI-D-13-00480.1.

Liebmann, B., and C. A. Smith, 1996: Description of a complete (interpolated) outgoing longwave radiation dataset. *Bull. Amer. Meteor. Soc.*, **77**, 1275–1277.

Lin, H., G. Brunet, and J. Derome, 2008: Forecast skill of the Madden–Julian oscillation in two Canadian atmospheric

models. *Mon. Wea. Rev.*, **136**, 4130–4149, doi:10.1175/2008MWR2459.1.

Liu, P., 2014: MJO structure associated with the higher-order CEOF modes. *Climate Dyn.*, **43**, 1939–1950, doi:10.1007/s00382-013-2017-0.

——, and Coauthors, 2009: An MJO simulated by the NICAM at 14- and 7-km resolutions. *Mon. Wea. Rev.*, **137**, 3254–3268, doi:10.1175/2009MWR2965.1.

Lorenz, E. N., 1956: Empirical orthogonal functions and statistical weather prediction. Scientific Rep. 1, Statistical Forecasting Project, Air Force Research Laboratories, Office of Aerospace Research, USAF, Bedford, MA. 49 pp.

Madden, R. A., and P. R. Julian, 1971: Detection of a 40–50 day oscillation in the zonal wind in the tropical Pacific. *J. Atmos. Sci.*, **28**, 702–708, doi:10.1175/1520-0469(1971)028<0702:DOADOI>2.0.CO;2.

——, and ——, 1972: Description of global-scale circulation cells in the tropics with a 40–50 day period. *J. Atmos. Sci.*, **29**, 1109–1123, doi:10.1175/1520-0469(1972)029<1109:DOGSCC>2.0.CO;2.

Maloney, E. D., and D. L. Hartmann, 1998: Frictional moisture convergence in a composite life cycle of the Madden–Julian oscillation. *J. Climate*, **11**, 2387–2403, doi:10.1175/1520-0442(1998)011<2387:FMCIAC>2.0.CO;2.

Miura, H., M. Satoh, T. Nasuno, A. T. Noda, and K. Oouchi, 2007: A Madden–Julian oscillation event realistically simulated by a global cloud-resolving model. *Science*, **318**, 1763–1765, doi:10.1126/science.1148443.

North, G. R., T. L. Bell, R. F. Cahalan, and F. J. Moeng, 1982: Sampling errors in the estimation of empirical orthogonal functions. *Mon. Wea. Rev.*, **110**, 699–706, doi:10.1175/1520-0493(1982)110<0699:SEITEO>2.0.CO;2.

Rayner, N. A., D. E. Parker, E. B. Horton, C. K. Folland, L. V. Alexander, D. P. Rowell, E. C. Kent, and A. Kaplan, 2003: Global analyses of sea surface temperature, sea ice, and night marine air temperature since the late nineteenth century. *J. Geophys. Res.*, **108**, 4407, doi:10.1029/2002JD002670.

Roundy, P. E., 2015: On the interpretation of EOF analysis of ENSO, atmospheric Kelvin waves, and the MJO. *J. Climate*, **28**, 1148–1165, doi:10.1175/JCLI-D-14-00398.1.

Rui, H., and B. Wang, 1990: Development characteristics and dynamic structure of tropical intraseasonal convection anomalies. *J. Atmos. Sci.*, **47**, 357–379, doi:10.1175/1520-0469(1990)047<0357:DCADSO>2.0.CO;2.

Slingo, J. M., and Coauthors, 1996: Intraseasonal oscillation in 15 atmospheric general circulation models: Results from an AMIP diagnostic subproject. *Climate Dyn.*, **12**, 325–357, doi:10.1007/BF00231106.

Straub, K. H., 2013: MJO initiation in the real-time multivariate MJO index. *J. Climate*, **26**, 1130–1151, doi:10.1175/JCLI-D-12-00074.1.

Ventrice, M. J., M. C. Wheeler, H. H. Hendon, C. J. Schreck III, C. D. Thorncroft, and G. N. Kiladis, 2013: A modified multivariate Madden–Julian oscillation index using velocity potential. *Mon. Wea. Rev.*, **141**, 4197–4210, doi:10.1175/MWR-D-12-00327.1.

Waliser, D., and Coauthors, 2009: MJO simulation diagnostics. *J. Climate*, **22**, 3006–3030, doi:10.1175/2008JCLI2731.1.

Wang, L., K. Kodera, and W. Chen, 2012: Observed triggering of tropical convection by a cold surge: Implications for MJO initiation. *Quart. J. Roy. Meteor. Soc.*, **138**, 1740–1750, doi:10.1002/qj.1905.

Webster, P. J., and R. Lukas, 1992: TOGA COARE: The Coupled Ocean–Atmosphere Response Experiment. *Bull. Amer. Meteor. Soc.*, **73**, 1377–1416, doi:10.1175/1520-0477(1992)073<1377:TCTCOR>2.0.CO;2.

Weickmann, K. M., G. R. Lussky, and J. E. Kutzbach, 1985: Intraseasonal (30–60 day) fluctuations of outgoing longwave radiation and 250 mb streamfunction during northern winter. *Mon. Wea. Rev.*, **113**, 941–961, doi:10.1175/1520-0493(1985)113<0941:IDFOOL>2.0.CO;2.

Wheeler, M. C., and G. N. Kiladis, 1999: Convectively coupled equatorial waves: Analysis of clouds and temperature in the wavenumber–frequency domain. *J. Atmos. Sci.*, **56**, 374–399, doi:10.1175/1520-0469(1999)056<0374:CCEWAO>2.0.CO;2.

——, and H. H. Hendon, 2004: An all-season real-time multivariate MJO index: Development of an index for monitoring and prediction. *Mon. Wea. Rev.*, **132**, 1917–1932, doi:10.1175/1520-0493(2004)132<1917:AARMMI>2.0.CO;2.

Wolding, B. O., and E. D. Maloney, 2015: Objective diagnosis and the Madden–Julian oscillation. Part I: Methodology. *J. Climate*, **28**, 4127–4140, doi:10.1175/JCLI-D-14-00688.1.

Yoneyama, K., C. Zhang, and C. Long, 2013: Tracking pulses of the Madden–Julian oscillation. *Bull. Amer. Meteor. Soc.*, **94**, 1871–1891, doi:10.1175/BAMS-D-12-00157.1.

Zhang, C., 2005: Madden-Julian Oscillation. *Rev. Geophys.*, **43**, RG2003, doi:10.1029/2004RG000158.

——, 2013: Madden–Julian Oscillation: Bridging weather and climate. *Bull. Amer. Meteor. Soc.*, **94**, 1849–1870, doi:10.1175/BAMS-D-12-00026.1.

Zhang, Q., and H. van den Dool, 2012: Relative merit of model improvement versus availability of retrospective forecasts: The case of climate forecast system MJO prediction. *Wea. Forecasting*, **27**, 1045–1051, doi:10.1175/WAF-D-11-00133.1.